Supplementary Information for

Enhanced power density in zero-vacuum-gap thermophotovoltaic devices

Mohammad Habibi[a,†], Sai C. Yelishala[a,†], Yunxuan Zhu[a], Eric J. Tervo[b,c], Myles A. Steiner[b], and Longji Cui[a,d,*]

[a] Paul M. Rady Department of Mechanical Engineering, University of Colorado Boulder, CO 80309, USA.

[b] National Renewable Energy Laboratory, Golden, CO 80401, USA

[c] Department of Electrical and Computer Engineering and Department of Mechanical Engineering, University of Wisconsin, Madison, WI 53706, USA

[d] Materials Science and Engineering Program and Center for Experiments on Quantum Materials, University of Colorado Boulder, CO 80309, USA

[†] These authors contributed equally.

[*] Lead contact. Correspondence: longji.cui@colorado.edu

Theoretical modelling and calculation methods

Radiative thermal transport in multi-layered TPV structures. To calculate the radiative energy exchange between the hot emitter and PV cell in different TPV schemes including far-field, near-field and zero-vacuum-gap TPVs, we applied a theoretical model based on fluctuational electrodynamics[1,2] in which the emitter is modeled as a collection of fluctuating thermal dipole sources. The fluctuation-dissipation theorem is used to obtain the correlation intensity of these fluctuating dipoles. A scattering matrix method is applied to calculate dyadic Green's functions, which are then used to determine the Poynting flux at a position relative to the emitting layer. The total thermal radiation that reaches the PV cell is obtained by $Q_{rad} = \int_0^\infty q(\omega).A.d\omega$ where A is the area of the PV cell, ω is the photon frequency, and $q(\omega)$ is the net spectral radiation heat flux between emitter and PV cell is determined by[3,4]

$$q(\omega) = \frac{\theta(\omega, T_e) - \theta(\omega, T_r)}{\pi^2} \int_0^\infty dk_\rho . G_\tau(\omega, k_\rho, T) \tag{1}$$

where *θ(ω,T)* represents the average energy of a Planck oscillator at a temperature *T* and frequency *ω*, and k_ρ is the parallel wavevector. G_τ is the energy transmission coefficient which is dependent on wavelength and wavevector and can be obtained as follows:

$$G_\tau = \left(1 - \left(\frac{n_a}{n_g}\right)^2\right) Re \left\{i\varepsilon''_e(\omega)k_\rho k_v^2 \int dV \left(g_{\rho\rho}^E . g_{\theta\rho}^{H*} + g_{\rho z}^E . g_{\theta z}^{H*} - g_{\theta\theta}^E . g_{\rho\theta}^{H*}\right)\right\} \tag{2}$$

where g^E and g^H denote the Weyl components of the electric and magnetic dyadic Green's functions in three coordination directions of ρ, θ, and z. *V* is the volume of the emitter. n_a and n_g are the refractive index of air/vacuum and the dielectric spacer, respectively. ε''_e is the imaginary part of the dielectric function of the emitter. It should be noted that the above equations can be applied to any TPV device and provide a universal approach to predict the performance of the TPV devices studied in this work. The calculated G_T and the associated spectral power distribution are plotted in Fig. 1d and 1e. The optical properties of InGaAs and the emitter materials can be obtained from refs [5,6]. The optical properties of the fused quartz[7] including transmissivity and absorption coefficient used in this experiment are shown in Fig. S1. Fused quartz is transparent from 0.5 to 2 μm, as indicated by its transmissivity and absorption coefficient. Within this range, the reflection of fused quartz reduces its transmissivity by approximately 10%.
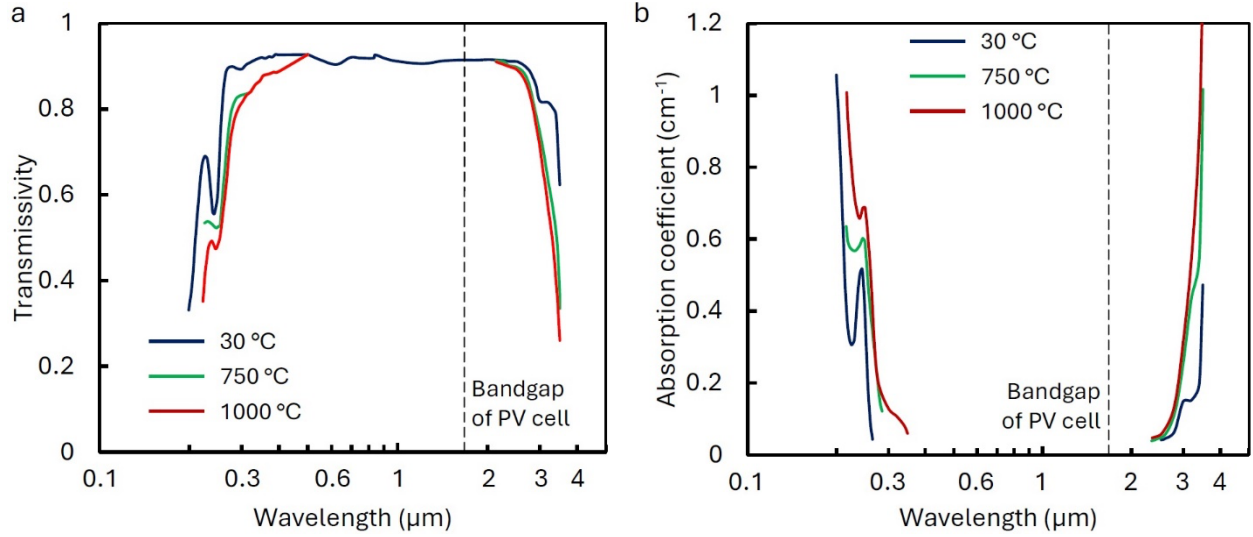
Fig. S1. Optical properties of fused quartz. a. transmissivity and b. absorption spectrum of fused quartz for 30, 750 and 1000 °C. The broken line is the bandgap of the InGaAs PV cell.

Modelling power generation in thin film PV cell. The current-voltage (J-V) characteristics of the TPV devices without illumination are formulated as $J = J_{diff} + J_{SRH} + J_{sh}$ [8], where each term represents a different component contributing to the total current density. The diffusion current, J_{diff}, is defined by $J_{diff} = J_0 \times [exp(qV/(kT)) - 1]$, where J_0 represents the saturation current that can be extrapolated from the forward linear region of a log (J) versus V plot under dark conditions. The Shockley-Read-Hall generation and recombination current, J_{SRH}, is approximated by $J_{SRH} = J_{GR} \times [exp(qV/(2kT)) - 1]$, where J_{GR} can be obtained from the forward log (J) versus V plot in the dark and is given by $J_{SRH} \approx J_{GR} = qn_iW/\tau_{SRH}$, with n_i being the intrinsic doping concentration of the active region, W the depletion width, and τ_{SRH} the Shockley-Read-Hall lifetime. The shunt current, J_{sh}, is given by $J_{sh} = V/R_{sh}$, where R_{sh} is the shunt resistance. Under high current, the contribution from series resistance R_s is pronounced, therefore V is replaced by $(V - J \cdot R_s)$ in the above formulas. When the PV cell is under illumination, the J-V characteristic is described by $J = J_{diff} + J_{SRH} + J_{sh} - J_{ph}$, where J_{ph} represents the photocurrent density. Using these parameters, *J-V* curves can be simulated for various J_{ph} levels. To calculate the photocurrent, we applied a Minority Carrier Separation (MCS) model[4,9] in which the PV cell is divided into *p*-doped, depletion, and *n*-doped regions for separate analysis. Photocurrent generation from the PV cell is obtained by numerically solving the steady-state continuity equation to model the carrier transport in a single *P-N* junction[4,9]. After obtaining the photocurrent density, the *J-V* characteristics of the PV cell are identified, and fill factor and power generation ($P = FF.J_{SC}.V_{OC}$) can be calculated.

Energy conversion efficiency. The energy conversion efficiency can be obtained via $\eta_{TPV} = SE \cdot IQE \cdot VF \cdot FF$, where $SE \cdot IQE$ can be obtained by[10]

$$SE \cdot IQE = \frac{\omega_{bg} \cdot \int_{\omega_{bg}}^{\infty} q(\omega) \cdot IQE \cdot d\omega}{\int_{0}^{\infty} q(\omega) \cdot \omega \cdot d\omega} \tag{3}$$

where ω_{bg} is bandgap frequency and IQE is internal quantum efficiency calculated from the MCS model[4,9]. VF is defined as $qV_{OC}/\hbar\omega_{bg}$ where V_{OC} is the open-circuit voltage, q is electron charge, and $\hbar$ is Planck's constant. The FF can be obtained by $FF = (J_{mp} \cdot V_{mp})/(J_{SC} \cdot V_{OC})$ where J_{mp} and V_{mp} are the J-V at the optimum power point and J_{SC} is the short-circuit current generation density.
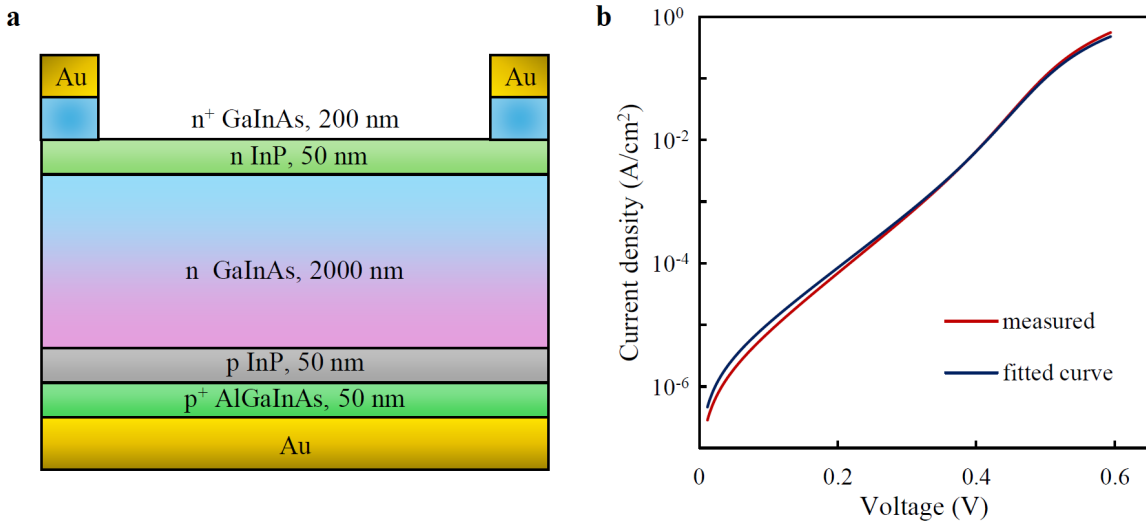

Fig. S2. Single-junction InGaAs cell structure and measured J-V characteristics. a. Schematic of the structure of a single rear-heterojunction InGaAs Cell. Non-absorber layers are designed to be minimally thick to reduce parasitic absorption of photons both above and below the bandgap. b. Measured and fitted dark J-V characteristics of the PV cell.

Zero-vacuum-gap vs. light-pipe TPV

Here we note the similarities and major differences between zero-vacuum-gap TPV and a historical far-field TPV concept called "light-pipe TPV", which we adopted in our far-field measurements to eliminate the effect of view factor in both TPV schemes and allow a fair comparison between the schemes. Fig. S3 shows the schematics for the light-pipe TPV and zero-vacuum-gap TPV. Briefly, in response to the need for an efficient TPV emitter, the light-pipe TPV concept was proposed in1990s[11]. In the light-pipe TPV design, a non-absorbing optical waveguide (i.e., a solid dielectric intermediate layer) is attached to the hot thermal emitter to channel most of the radiation to the PV via the increased view factor between the emitter and the PV cell. The increased view factor results in a dramatically increased power density. Similar to zero-vacuum-gap TPV, the favored optical waveguide material in light-pipe TPV have low thermal conductivity to provide insulation between the emitter and the PV cell so a number of materials including fused silica and undoped crystalline yttrium alumina garnet (YAG) have been considered as good candidates. However, light-pipe TPV maintains the crucial air-gap feature between the waveguide and PV cell, which makes it one variant of far-field TPV, which is fundamentally limited by the vacuum blackbody limit in the presence of a gap. Here it should be noted that since the pioneering study, there has been theoretical work[12,13] that discussed the power enhancement and efficiency improvement when an intermediate layer fills the gap between the emitter and the PV cell. However, to the best of our knowledge, there has been no experimental demonstration of a practical TPV device without any air or vacuum gaps. In this work, we categorize light-pipe TPV within the domain of far-field TPV to distinguish these concepts.
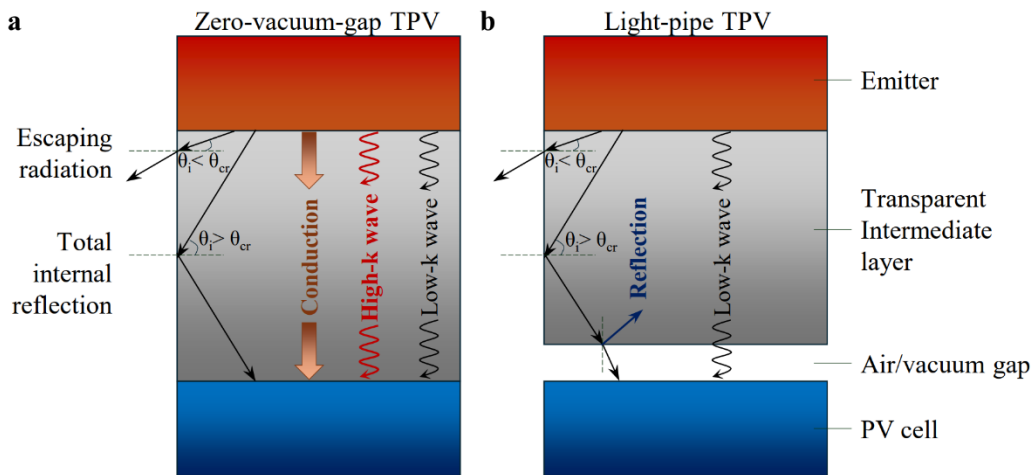

Fig. S3. Comparison between zero-vacuum-gap TPV and light-pipe TPV. In zero-vacuum-gap TPV the intermediate layer is connected to the emitter and the PV cell, while in light-pipe TPV there is an air gap between the transparent intermediate layer and PV cell.

Fabrication of thin film InGaAs PV cell and Characterization

Cell fabrication. The thin film InGaAs PV cells used in this study are fabricated using metalorganic vapor phase epitaxy, renowned for producing high-quality, single-crystal III-V semiconductors as shown in Fig. S2. Starting with a 2-inch indium phosphide (InP) substrate, we grow all epitaxial layers with uniform lattice constants to minimize defects. The cells were constructed with an inverted design: the front contact layer is deposited first, followed by subsequent layers, with the back contact last. This structure allows for the deposition of a back reflector after growth, and the cell is then bonded to a silicon carrier. The InP substrate is chemically removed, leaving only the thin epitaxial layers. Standard photolithography, electroplating, and wet chemical etching techniques are used to fabricate each cell, with electroplated back reflector and front grid with thicknesses of around 3 µm. Inverted growth enables the production of lightweight, flexible thin-film cells and supports cost-effective substrate reuse methods like epitaxial liftoff or spalling. Each cell's light and dark area measures 0.1005 cm^2 and 0.1156 cm^2, respectively.

Cell characteristics. The bandgap of the fabricated InGaAs cell is 0.74 eV. From the fitted dark J-V curve (see Fig. S2), parameters for the PV cell are determined as follows: $J_0 = 0.5\ nAcm^{-2}$, $J_{GR} = 1.77\ \mu Acm^{-2}$, $R_{sh} > 10^6$ Ω, and $R_s = 0.14\ \Omega cm^{-2}$. In comparison, the cell recently fabricated and reported with high efficiency[10] using a similar procedure has a 20 times smaller series resistance of 0.0065 Ωcm^{-2}, likely due to much thicker back reflector and front grids. Such high series resistance reduces the efficiency of our current PV cell especially when the current density is high at high temperatures. Electrical characteristics are assessed using J-V measurements under illumination. As emitter temperature rises, so does the radiation incident on the cell in both intensity and photon energy, leading to an increased photocurrent. Key parameters such as the short-circuit current, FF, and open-circuit voltage are derived from the measurements. The PV cell exhibits a robust open-circuit voltage of 0.55 V, with a short-circuit current of 154 mA/cm^2 in z-TPV with graphite as the emitter at 1133 K. Fig. S4 shows that the open-circuit voltage escalates with increasing radiation intensity. The FF remains relatively good at approximately 0.65 under elevated emitter temperatures, but it tends to decrease at very high current densities due to the high series resistance of our PV cell.

For the simulation of the optimized cell in fig 6a in the main text, we used series resistance of $R_s = 6.5\ m\Omega cm^{-2}$ based on Tervo et al.[10] work. Moreover, the other parameters that we used for the optimized cell are $J_0 = 0.705\ nAcm^{-2}$, and $J_{GR} = 0.966\ \mu Acm^{-2}$. For the optimized cell simulation, we assumed that the energy transmission loss of the high-k propagation waves is zero.

Characterization of zero-vacuum-gap TPV devices

J-V and power generation characterizations. The J-V characteristics under dark and various illumination conditions were measured using a Keithley 2401 SMU, which operates in a four-wire sensing mode. Measured short-circuit current and open-circuit voltage are plotted in Fig. S4, showing that zero-vacuum-gap TPVs, even with lower emitter temperatures, yield higher short-circuit current densities compared to the far-field counterpart. For instance, a zero-vacuum-gap TPV device operating at 1281 K produces 50% more current density than a far-field device using the same PV cell at 1316 K. Furthermore, the energy conversion efficiency of TPV can be obtained from the measured J-V characteristics, and the heat flux which is measured by the heat flux sensor underneath the PV cell. It should be noted that specific to zero-vacuum-gap TPV, the measured heat flux consists of several contributing factors including the absorbed thermal radiation within the PV cell, heat generation due to electron-hole recombination in the cell, and conduction heat transfer through the dielectric spacer layer.
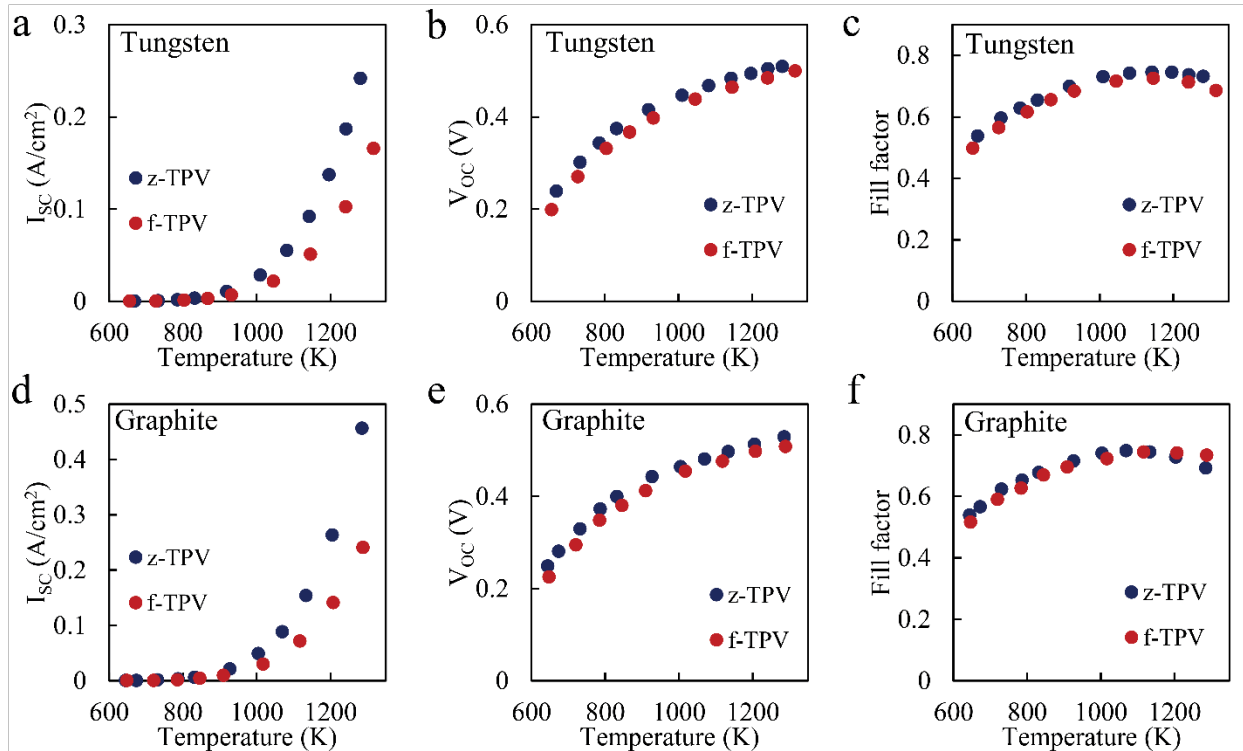

Fig. S4. Measured power generation performance of zero-vacuum-gap vs. far-field TPV. Short-circuit current, open-circuit voltage and fill factor of PV cell for two emitter materials: tungsten and graphite.

Figure S5 provides a detailed comparison of the thermal and electrical performance of the 2 cm and 10 cm zero-vacuum-gap TPV (z-TPV) devices. Fig. S5a presents the current-voltage (J-V) characteristics for the 2 cm spacer configuration, while fig. S5b shows the J-V characteristics for the 10 cm spacer. It can be observed that the current generation for the 10 cm spacer is approximately the same as that for the 2 cm spacer. Fig. S5c

illustrates the measured heat flux at equilibrium for both the 2 cm and 10 cm spacers, obtained using the heat flux sensor, showing that the heat transfer between the emitter and PV cell is higher for the z-TPV with the 2 cm spacer. Lastly, fig. S5d depicts the measured PV cell temperature for the 2 cm and 10 cm spacers, both with and without the HFS. The presence of the HFS increases the PV cell temperature due to the additional thermal resistance introduced between the PV cell and the heat sink. Without the HFS, the PV cell temperature remains below 27 °C for both the 2 cm and 10 cm spacer configurations.
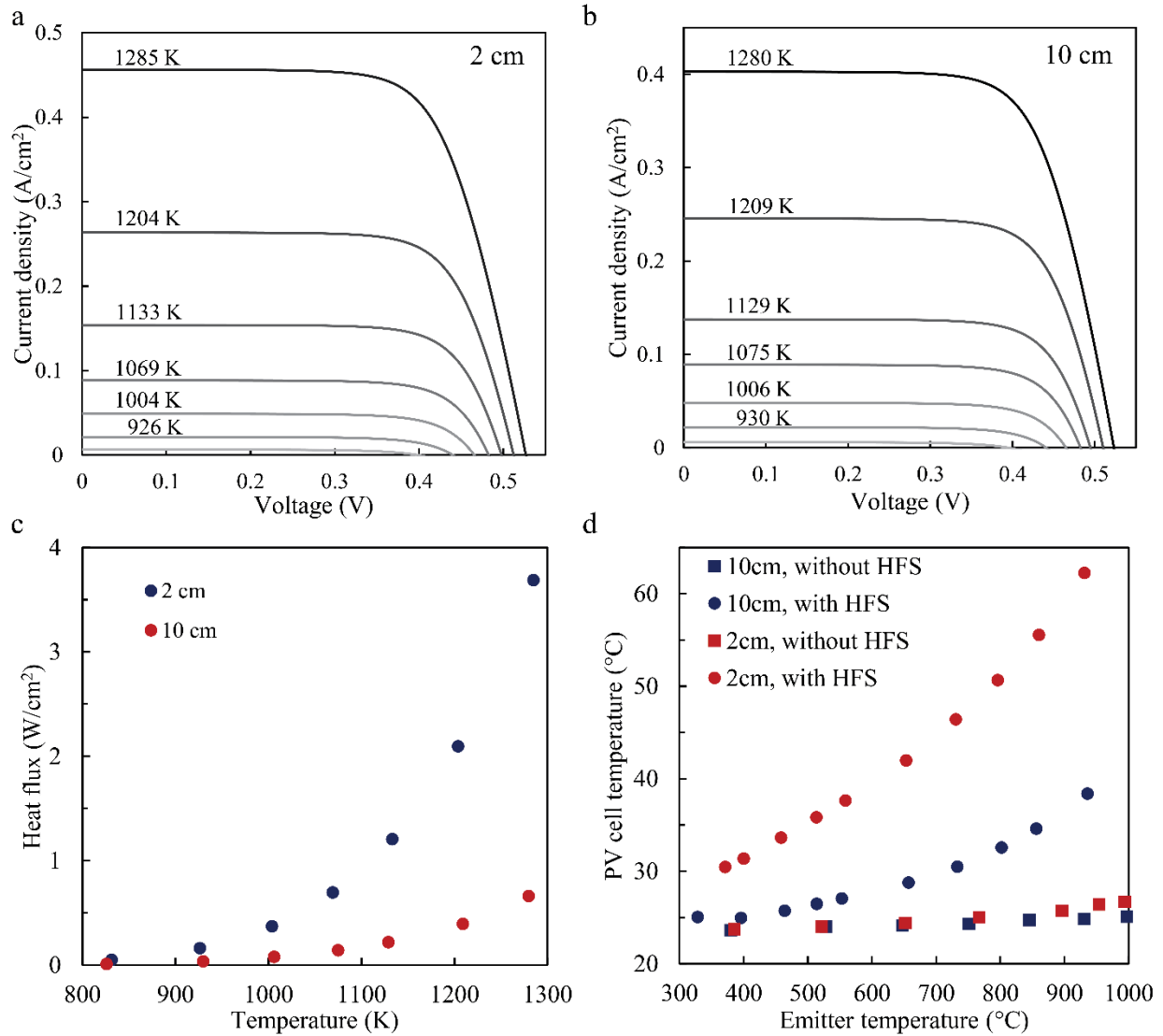

Fig. S5. Measured power current-voltage characteristic of zero-vacuum-gap with (a) 2 and (b) 10 cm fused quartz as the dielectric spacer. (c) Measured heat flux by HFS in zero-vacuum-gap with 2 and 10 cm fused quartz as the dielectric spacer. (d) Measured PV cell temperature with and without HFS in zero-vacuum-gap with 2 and 10 cm fused quartz as the dielectric spacer. The emitter material is graphite in all cases.

Effects of various energy loss mechanisms in zero-vacuum-gap TPV

Optical loss and effects of view factor. Fig. S6 illustrates the optical losses and small view factor effect due to the finite size of the PV cell used in this study and our proposed strategies to eliminate these losses in practical TPV applications. Specifically, with the long rod shaped dielectric spacer inserted between the emitter and PV cell, part of the thermal radiation with an incident angle (θ_i) smaller than the critical angle (θ_{cr}) can escape from the spacer layer, whereas the remaining radiation can be reflected and directed towards the PV cell. It can be calculated that the fraction of radiation that is reflected and guided toward the PV cell is $1 - \left(n_{air/vacuum}/n_{fused\ quartz}\right)^2$ [13,14]. Alternatively, Fresnel coefficients for reflection (r_{ga}) on the boundary between the dielectric spacer medium and air/vacuum can also be used to roughly estimate the fraction of escaped radiation. Specifically, the portion of the wave guided towards the PV cell can be obtained as $\cong \int_0^\infty |r_{ga}|^2 G_T.dk / \int_0^\infty G_T.dk$ where G_T is the transmission function in Eq. (1). Using this expression, we can calculate the percentage of thermal radiation into the PV cell is $\approx 53\%$, with $\approx 47\%$ escaped from the exposed surface of the dielectric spacer (fused quartz). The percentage of the escaped radiation is significantly reduced when the refractive index of dielectric spacer is increased. For example, for a-Si with a refractive index of 3.4, only 8.7% of the radiation escapes, while 91.3% of radiation is guided into the PV cell.
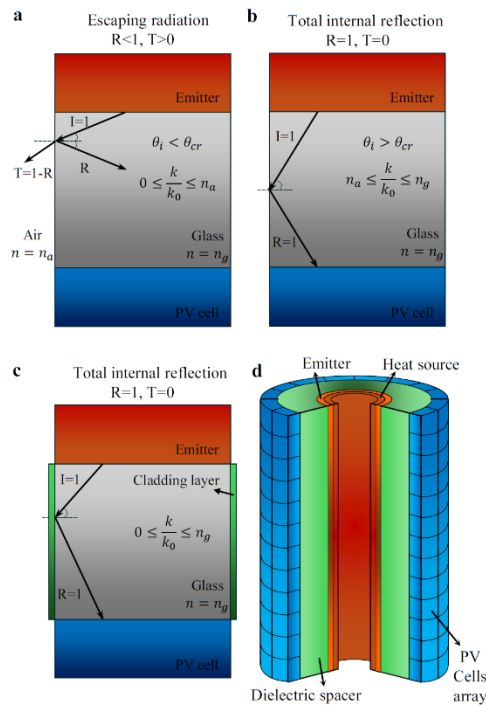

Fig. S6. Evaluation of optical losses in zero-vacuum-gap TPV and mitigation strategies. a, Pathways of thermal radiation in the dielectric spacer including escaped radiation and total internally reflected photons. b, two strategies to minimize the optical losses, including adding a cladding layer with high refractive index similar to a lossless optical fiber, and a cylindrical TPV structure that confines all photons within the TPV structure.

We note here that due to the limitation of our PV cell size and rod-shape experimental configuration, the above optical loss is inevitable, which effectively reduced the view factor of radiative energy exchange in the TPV device. However, these losses can be reduced by applying a cladding layer [15,16] around the dielectric spacer (Fig. S6c), similar to the method used to reduce the transmission losses in optical fibers. Alternatively, a cylinder-shaped TPV device (Fig. S6b), which has been commonly used for combustion-fueled TPV power generation and grid energy storage, can eliminate optical loss and allow all radiated energy to be channeled to the PV cell.

Effects of non-radiation (conduction and convection) losses. Due to the presence of the solid dielectric spacer, heat transfer pathways open for both heat conduction from emitter to PV cell and convection from the spacer layer to the ambient environment. In our experiment, we define energy conversion efficiency as the ratio of the generated power in the PV cell and the amount of heat that reaches to the PV cell which consists of both radiation and conduction. Following the same strategy adopted in recent high-efficiency TPV experiments, the total involved heat flux is measured directly by the heat flux sensor installed underneath the PV cell. By this definition, efficiency increases with increasing dielectric spacer length due to the suppressed conduction heat flux. However, as our experiments are performed in air, it should be noted that there are substantial convection losses from the high temperature heater side and from the dielectric spacer layer surface due to our single flat cell TPV configuration which exposes large areas of hot surface to the ambient. In practical applications, the TPV module can be configured into a cylindrical shape (as shown in Fig. S6d) which minimizes the convection losses from both the emitter and the dielectric spacer layer. As discussed above, a cylindrical TPV module also eliminates optical losses by confining all emitted photons from the emitter in the enclosed device structure. Therefore, we expect such a device structure to be adopted for large-scale applications to fully exploit the potential of zero-vacuum-gap TPV. Furthermore, comparing radiative heat transfer and heat conduction for different materials at different temperatures, we also used a cylindrical TPV structure, as shown in Fig. S7. We used finite volume method to calculate the heat conduction from the emitter to the PV cell.
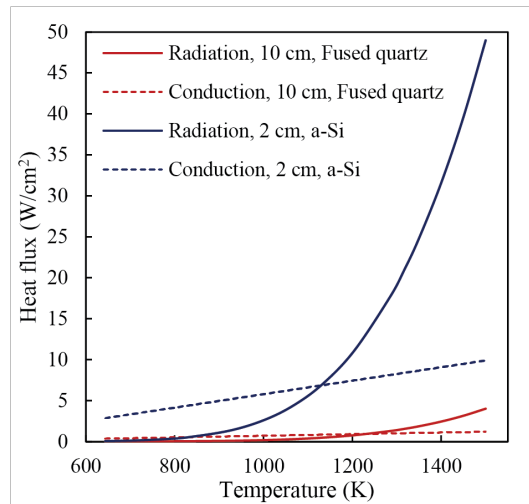
Fig. S7. Comparison between radiation and conduction heat fluxes in zero-vacuum-gap TPV for different materials. The calculations are based on 10-cm fused quartz spacer and 2-cm a-Si spacer as the dielectric spacers. The effect of conductive heat transfer diminishes at high temperatures.

Electrical losses. Inherent to the quality of the InGaAs cells, there are a number of electrical loss factors including series resistance and recombination for electron-hole generation. As shown in Fig.6a, these electrical loss mechanisms are responsible for our measured moderate energy conversion efficiency, in comparison with the recent demonstration of high efficiency in far-field TPV devices using InGaAs devices with optimized cell growth processes [10]. Further improvement of zero-vacuum-gap TPV efficiencies can be anticipated if similar optimization procedures can be applied to reduce series resistances and optimize the spectral efficiency of the cell. Indeed, our theoretical prediction has suggested that with the optimized PV cell parameters, the energy conversion efficiency of zero-vacuum-gap TPV can reach around 30% at a temperature of 1200 K (Fig. 6a), which could even outperform both far-field and near-field TPV devices.

Other optical losses in TPV devices. Other than the escaped thermal radiation from the dielectric spacer described above, there are other sources of optical losses which are responsible for our observed power enhancement ratio which is lower than the predicted value. The first source of optical loss comes from the potential miniature gaps between the deposited thermal emitter and the dielectric spacer. Unwanted air gaps between the emitter and the spacer could emerge due to mismatch in thermal expansion coefficient of the two

material at different temperatures. Another optical loss factor is due to the micro/nanoscale air bubbles trapped in optical epoxy. Moreover, due to the surface roughness of the PV cell and the existence of the grid
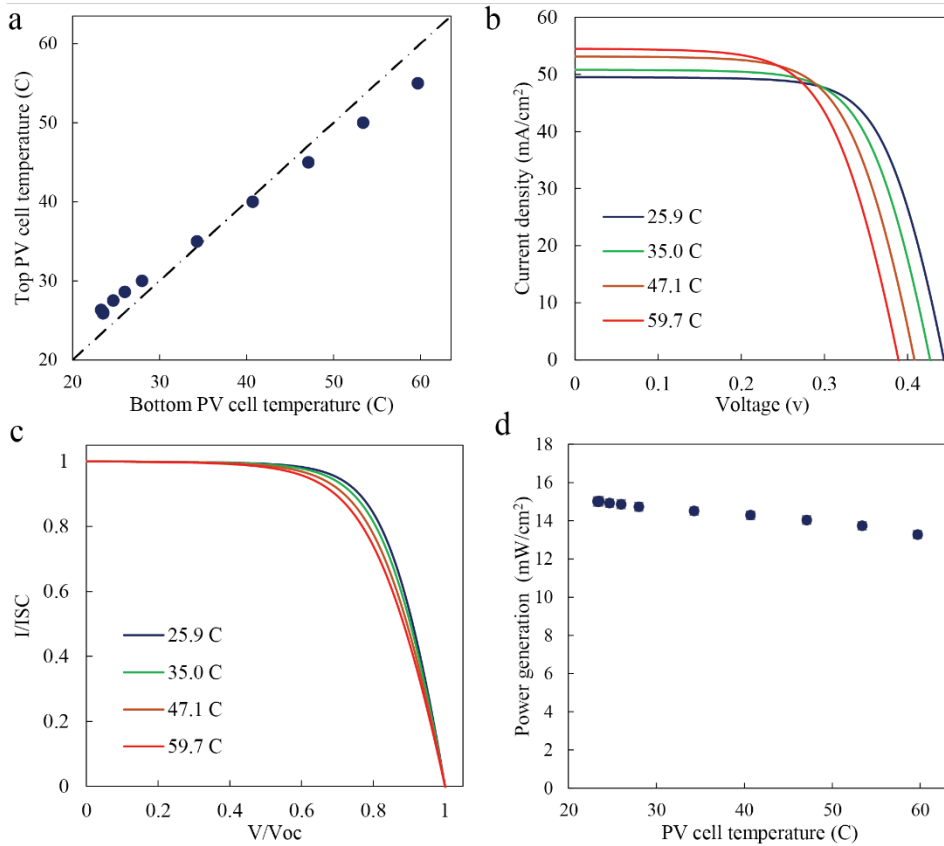

Fig. S8. The effect of PV cell temperature on measured zero-vacuum-gap TPV performance. a. Measured top and bottom temperature of the PV cell using two embedded thermocouples. b, measured J-V characteristics of the zero-vacuum-gap TPV device under different PV cell temperatures that are controlled by the cooling rate of the microchannel heat exchanger. c, Measured short-circuit current density and open-circuit voltage of the PV cell at different PV cell temperatures. d, Measured power densities of zero-vacuum-gap TPV at different PV cell temperatures.

lines, the applied optical epoxy might not fill completely the gaps, which could impede the transmission of high-k waves through the structure. In zero-vacuum-gap TPV systems, another optical loss occurs when sub-bandgap photons are absorbed by the dielectric spacer. These photons, with energies below the PV cell's bandgap, do not contribute to electricity generation and are instead converted to heat, reducing the system's efficiency. To minimize this loss, a selective emitter can be used to limit the emission of sub-bandgap radiation, thereby reducing photon absorption in the spacer. By emitting mainly above-bandgap photons, selective emitters enhance energy conversion efficiency. Various selective emitters developed for far-field TPV systems have demonstrated high efficiencies, and their integration into zero-vacuum-gap TPV systems offers a promising way to prevent type of optical loss and improve efficiency.[17,18]

We summarize several energy loss mechanisms that influence the performance of the zero-vacuum-gap TPV system as follows: Escaped radiation reduces both the generated power and radiative heat flux by

approximately one half. While this does not affect cell efficiency which only accounts for the energy conversion on the cell side by discarding the energy losses inside the spacer, it decreases the overall system efficiency, as radiation decreases but non-radiation heat transfer remains unchanged. Non-radiation thermal Losses increase the total heat load while reducing system efficiency. Since they do not affect the radiative flux directly, they have no impact on power generation. Optical losses of high-k waves reduce both the generated power and heat flux. This results in lower system efficiency. Below-bandgap absorption reduces the heat flux reaching the PV cell while increasing heat dissipation from the heater, reducing overall system efficiency. Electrical losses due to series resistance lower the generated power and reduce overall efficiency but do not impact heat flux.

The effect of PV cell heating on power generation. We have also performed measurements to show that the heating of PV cells has marginal influence on the performance of zero-vacuum-gap TPV devices. Specifically, we performed TPV tests under a fixed emitter temperature of 1027 K, and controlled the temperature of the PV cell to vary from 25 °C to 60 °C by changing the liquid cooling rate of the microchannel heat exchanger. Fig. S8 shows the measured PV cell temperature by the two embedded thin film thermocouples, one underneath the PV cell and another glued on the side of the cell. It can be seen from the J-V characteristics, that by increasing the PV cell temperature, the measured open-circuit voltage decreases but the short –circuit current density increases. To show how the fill factor varies, the non-dimensional J-V characteristic is shown in Fig. S8c. We found that the fill factor decreases as the cell temperature increases. The measured power density is shown in Fig. S8d. It can be seen that the decrease in power density with the increasing cell temperature is not significant with only ~13% of power loss when the cell temperature increases from 25.9 to 59.7 °C.

Zero-vacuum-gap & near-field TPV comparison

Both zero-vacuum-gap TPV and near-field TPV are promising approaches for achieving high power densities at moderate emitter temperatures. In Fig. S9, we compare the power generation densities of these two methods. We conducted simulations for near-field TPV using the same emitter and PV cell configuration as in our zero-vacuum-gap TPV experiment. The results show that the power performance of our fabricated zero-vacuum-gap TPV device is comparable to that of the near-field TPV device, with a vacuum gap of 175 nm, under the same temperature conditions.

This finding is significant, as it demonstrates that zero-vacuum-gap TPV can achieve similar power density to near-field TPV, without the challenges of creating and maintaining sub-wavelength vacuum gaps. Furthermore, near-field TPV systems, while efficient, are often limited by scalability issues due to the precise control required over the nanometer-scale gap between the emitter and the PV cell. In contrast, zero-vacuum-gap TPV leverages a dielectric spacer, which simplifies the fabrication and increases the system's robustness in practical applications.
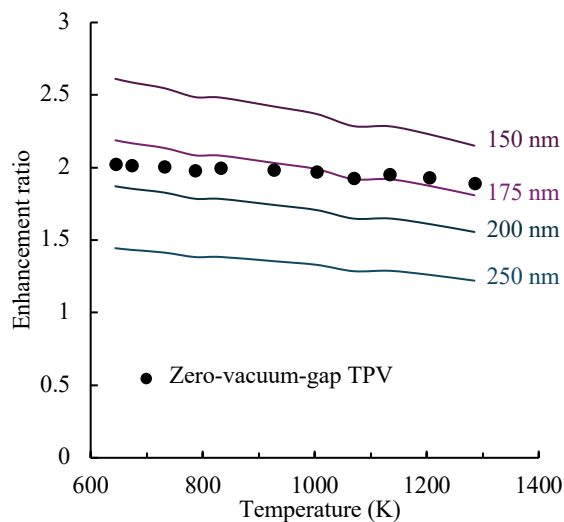
Fig. S9. The comparison between the enhancement ratio of zero-vacuum-gap TPV (experiment) and the simulated near-field TPV for different vacuum gap sizes. All cases have the same emitter and PV cell.

Consideration of other dielectric spacer materials

As a proof-of-concept, our experiments used fused quartz as the dielectric spacer material. It should be noted that fused quartz is not optimal for zero-vacuum-gap TPV due to its moderate refractive index and below-bandgap optical losses which reduce the system efficiency of the device. Alternatively, other materials such as a-Si, GaAs, ZnSe, and crystalline YAG which have higher refractive index and broader spectral transparency can be selected to achieve very high-power density enhancement while maintaining the high efficiency. One issue to use other materials for zero-vacuum-gap TPV is that different device fabrication methods are required. However, we note that this does not pose significant technical challenges since in principle one can use any dielectric spacer material with fabricated end-patterns so the dielectric spacer layer and the PV cell can be precisely aligned using common lithography and mask aligning techniques to produce a zero-vacuum-gap device.

References:

1. Rytov, S. M., Kravtsov, Y. A. & Tatarskii, V. I. *Principles of Statistical Radiophysics 3: Elements of Random Fields*. (Springer Berlin, Heidelberg, 1989).

2. Joulain, K., Mulet, J. P., Marquier, F., Carminati, R. & Greffet, J. J. Surface electromagnetic waves thermally excited: Radiative heat transfer, coherence properties and Casimir forces revisited in the near field. *Surf Sci Rep* **57**, 59–112 (2005).

3. Francoeur, M., Pinar Mengüç, M. & Vaillon, R. Solution of near-field thermal radiation in one-dimensional layered media using dyadic Green's functions and the scattering matrix method. *J Quant Spectrosc Radiat Transf* **110**, 2002–2018 (2009).

4. Habibi, M. & Cui, L. Modelling and performance analysis of a novel thermophotovoltaic system with enhanced radiative heat transfer for combined heat and power generation. *Appl Energy* **343**, 121221 (2023).

5. Mittapally, R. *et al*. Near-field thermophotovoltaics for efficient heat to electricity conversion at high power density. *Nat Commun* **12**, 4364 (2021).

6. Newquist, L. A., Querry, M. R., Alexander, R. W., Ordal, M. A. & Bell, R. J. Optical properties of Al, Fe, Ti, Ta, W, and Mo at submillimeter wavelengths. *Applied Optics* **27**, 1203–1209 (1988).

7. Shackleford, W. L., Bass, C. D. & Beder, E. C. Transmissivity and Absorption of Fused Quartz Between 0.22 μ and 3.5 μ from Room Temperature to 1500°C. *Applied Optics* **10**, 2263–2268 (1971).

8. Fan, D. *et al*. Near-perfect photon utilization in an air-bridge thermophotovoltaic cell. *Nature* **586**, 237–241 (2020).

9. Francoeur, M., Vaillon, R. & Meng, M. P. Thermal impacts on the performance of nanoscale-gap thermophotovoltaic power generators. *IEEE Transactions on Energy Conversion* **26**, 686–698 (2011).

10. Tervo, E. J. *et al*. Efficient and scalable GaInAs thermophotovoltaic devices. *Joule* **6**, 2566–2584 (2022).

11. Goldstein, M. K., DeShazer, L. G., Kushch, A. S. & Skinner, S. M. Superemissive light pipe for TPV applications. *AIP Conf Proc* **401**, 315–326 (1997).

12. Bauer, T., Forbes, I., Penlington, R. & Pearsall, N. Heat transfer modelling in thermophotovoltaic cavities using glass media. *Solar Energy Materials and Solar Cells* **88**, 257–268 (2005).

13. Chubb, D. L. Light Pipe Thermophotovoltaics (LTPV). *AIP Conf Proc* **890**, 297–316 (2007).

14. Chubb, D. L. Emittance theory for cylindrical fiber selective emitter. *AIP Conf Proc* **460**, 463–471 (1999).

15. Bauer, T., Forbes, I., Penlington, R. & Pearsall, N. Heat Transfer Modelling of Glass Media within TPV Systems. *AIP Conf Proc* **738**, 153–161 (2004).

16.   Goldstein, M. K. Superemissive light pipes and photovoltaic systems including same. (1995).

17.   Pfiester, N. A. & Vandervelde, T. E. Selective emitters for thermophotovoltaic applications. *physica status solidi (a)* **214**, 1600410 (2017).

18.   Woolf, D. N. *et al.* High-efficiency thermophotovoltaic energy conversion enabled by a metamaterial selective emitter. *Optica* **5**, 213–218 (2018).